

**Modeling the Shape and Evolution of Normal-Fault
Facets**

Gregory E. Tucker^{1*}, Frog^{2,1,2}, Frog³

¹Cooperative Institute for Research in Environmental Sciences and Department of Geological Sciences,
University of Colorado, Boulder, Colorado, USA.

²Frog Pond.

³Toad Pond.

Key Points:

- What, you're too impatient to read the abstract?

*Current address, McMurdo Station, Antarctica

Corresponding author: A. B. Smith, email@address.edu

10 **Abstract**

11 this is a highly abstract paper

12 **1 Introduction**

13 Mountain ranges in extensional tectonic settings often display fault scarps adorned
 14 with facets: steep, basin-facing hillslopes that follow the surface trace of the bounding
 15 fault and mark the transition from footwall to hangingwall (Figure 1). In many cases,
 16 dissection of a footwall range by transverse streams creates flights of triangular facets:
 17 facet slopes that are flanked by V-shaped transverse valleys, which present a triangu-
 18 lar shape when viewed from the adjacent basin (see especially Figures 1a,e,i). In other
 19 settings, facets may be trapezoidal in profile, or even compose a more or less continu-
 20 ous surface along a weakly dissected footwall range [e.g., *Wallace*, 1978] (Figure 1g,h).

21 The aim in this paper is to explore the sculpting of facet cross-sectional profiles,
 22 using a numerical process-based model as an interpretive tool. We examine the extent
 23 to which the model can account for the diversity in facet morphology, and in particu-
 24 lar diversity in slope angle, regolith cover, profile shape, and presence or absence of a slope
 25 break across the range-bounding fault. We also use the model to frame testable predic-
 26 tions for the relationship between facet morphology, erosion rate, and fault slip rate.

27 **2 Background**

28 Facets have intrigued geologists since at least the late 19th century, when early sur-
 29 vey expeditions of the American west (and, later, railroad construction) provided access
 30 to the spectacular terrain of the Basin and Range physiographic province. Among the
 31 first published remarks and illustrations on facet geomorphology in the western USA were
 32 those of *Davis* [1903, 1909]. Both he and *Gilbert* [1928] viewed facets as exhumed fault
 33 planes, with only minor modification by erosion. Later workers, however, noted a dis-
 34 crepancy between the dip angle of facets and of the fault planes beneath. Where facets
 35 often dip between 20° and 35° [*Davis*, 1903, 1909; *Pack*, 1926; *Blackwelder*, 1928; *Gilluly*,
 36 1928; *Fuller*, 1931; *Anderson*, 1977; *Wallace*, 1978; *Menges*, 1990; *Petit et al.*, 2009; *Wilkin-
 37 son et al.*, 2015], the bedrock fault planes below commonly form angles of 60° to 70° with
 38 respect to the horizontal [*Schneider*, 1925; *Pack*, 1926; *Blackwelder*, 1928; *Gilluly*, 1928;
 39 *Fuller*, 1931; *Wallace*, 1978; *Wilkinson et al.*, 2015]. The difference in dip between a nor-

40 mal fault plane and the facets above it implies that facets, despite their often strikingly
41 planar form, are erosionally modified features [Pack, 1926; Gilluly, 1928]. Gilluly [1928],
42 in his work on the Oquirrh Range (Utah, USA), pointed out an interesting implication
43 of this erosional modification: “as the dip of the fault averages more than 60 degrees along
44 this part of the range front, a wedge having an apical angle of 30 to 40 degrees has ev-
45 idently been removed from each facet.” In other words, because the tip of a facet gets
46 exposed to erosion earlier than the base, it undergoes more cumulative erosion. In this
47 sense, the tip of a facet may be considered “geomorphically older” than the base [Gilbert,
48 1928; Wallace, 1978; Menges, 1990].

49 An unusually well-documented example of the contrast between fault plane and facet
50 morphology comes from a study of the Campo Felice fault in the Italian central Apen-
51 nines by Wilkinson *et al.* [2015]. Detailed maps of the Campo Felice fault plane obtained
52 from terrestrial laser scans of the bedrock fault scarp, together with ground-penetrating
53 radar images of the fault plane in the subsurface, revealed the fault dip to be $57 \pm 4^\circ$, whereas
54 the facet surface above the exposed fault plane dips at $40 \pm 5^\circ$ and the debris below the
55 fault trace dips at $36 \pm 3^\circ$. Along the Campo Felice, therefore, Giluly’s “removed wedge”
56 would have an apical angle of about 17° .

57 Facets show a wide diversity in morphology. Although the dip angles of many facets
58 range between 20° and 35° , facets have been reported to have dips as low as several de-
59 grees [e.g., Menges, 1990; Struble *et al.*, in review] or as high as $\geq 40^\circ$ [e.g., Wilkinson
60 *et al.*, 2015; Struble *et al.*, in review]. Their apices may vary in height from tens to hun-
61 dreds of meters. Some facets are more or less continuously mantled in soil, as for exam-
62 ple those along a portion of the Sangre de Cristo Range in New Mexico, USA studied
63 by Menges [1990], as well as on some facets along the eastern margin of the American
64 Basin and Range (Figure 1d,f,i). Others, including facets developed on carbonate rocks
65 in the Italian central Apennines, are rocky, with a shallow, discontinuous colluvium [Tucker
66 *et al.*, 2011] (Figure 1g,h). The longitudinal profiles of facets may be planar or convex-
67 upward. Some faceted mountain fronts display a clear break in slope between the base
68 of the facets and an adjacent colluvial apron (Figure 1g). For example, hangingwall col-
69 luvial slopes surveyed by Bubeck *et al.* [2015] in the Apennines showed slope angles of
70 $20\text{--}25^\circ$. Along other mountain fronts, the basal colluvium dips at about the same an-
71 gle as the facet above, with the contact between the two sometimes marked by a fault
72 scarp (Figure 1h), and sometimes obscure (Figure 1i).

The diversity in facet morphology raises the question of whether facets may encode useful information about tectonic processes, as several studies have suggested. *Hamblin* [1976] and *Anderson* [1977] identified flights of facet-like surface the Wasatch Front (Utah, USA) separated by bench-like spurs, and interpreted these as reflecting alternating episodes of rapid slip and tectonic quiescence. *Menges* [1990] noted that facets along the southern Sangre de Cristo Range tend to be steeper and taller toward the middle of fault segments, as opposed to zones of overlap between adjacent segments. *DePolo and Anderson* [2000] compiled morphologic data on 45 faults with independent slip-rate estimates in the arid to semi-arid environment of the Great Basin, USA. Faults with a slip rate in excess of a few 10s of microns per year were associated with facets, and among these, *DePolo and Anderson* [2000] demonstrated a correlation between slip rate and facet height. In a study of facets along four segments of the Wasatch fault system, *Zuchiewicz and McCalpin* [2000] noted multiple potential controls on facet geometry, including lithology, but considered slip rate to be the primary control. In laboratory experiments by *Strak et al.* [2011], facet angle increased with slip rate up to a limiting threshold angle. By contrast, *Densmore et al.* [1998] and *Ellis et al.* [1999] suggested on the basis of numerical model experiments that facet erosion might be controlled chiefly by bedrock landsliding, such that facet angle represents a threshold angle for stability that does not correlate with slip rate.

If facets take shape through a collaboration between tectonics and erosion, then it stands to reason that their morphology might also encode useful information about rates of geomorphic processes. *Menges* [1990] noted, for example, that the degree of soil development generally increases upslope on facets along the southern Sangre de Cristo Range. Using a simple geometric model, *Tucker et al.* [2011] noted that the difference in dip angle between a facet and its basal fault—in other words, the apical angle of Gilluly’s wedge of missing rock—could be related quantitatively to the ratio of the rates of fault slip and facet erosion, according to:

$$\beta = \alpha - \theta = E/V, \quad (1)$$

where α is the fault dip angle, θ is the facet dip angle, E is the slope-normal facet erosion rate, and V is the fault slip rate. The concept is illustrated in Figure 2. One implication of the geometry illustrated in Figure 2 is that if one knew the fault slip rate and the fault dip, one could estimate the erosion rate (averaged over the age of the facet).

104 Conversely, independent knowledge of the erosion rate would allow estimation of the slip
 105 rate.

106 The geometric view of facets as surfaces that erode as they emerge from below ground
 107 leads to the question of what factors determine the erosion rate on a normal-fault facet—
 108 and this in turn raises the questions of what are the controlling processes. *Wallace* [1978]
 109 hypothesized that fault scarps created by tectonic offset should relax relatively quickly
 110 from the initial fault dip to a more stable angle of 30 to 37°, and thereafter lay back much
 111 more slowly. *Densmore et al.* [1998] and *Ellis et al.* [1999] proposed, on the basis of nu-
 112 matical model experiments, that many facets form by bedrock landsliding, and that the
 113 facet surfaces essentially represent failure planes. *Petit et al.* [2009] questioned this in-
 114 terpretation, in part because of the scarcity of features such as head scarps and debris
 115 lobes that one would expect to be associated with bedrock landsliding. Our own obser-
 116 vations of facets in the Italian Apennines and the Wasatch fault system, USA, also lead
 117 us to support the view of *Petit et al.* [2009] that facets commonly undergo progressive
 118 weathering and erosion. *Menges* [1990] suggested that facets might be effectively transport-
 119 limited, yet the fact that some facets have extensive bedrock outcrops suggests that this
 120 is not always the case. Whereas *Menges* [1990] noted some evidence for slope wash, *Gilbert*
 121 [1928] argued that “rains accomplish little in the way of erosion... [due to] absorption
 122 and retardation by porous talus and in conditions unfavorable to concentration of flow.”
 123 Finally, variations in facet morphology and scale with lithology implies that facet ma-
 124 terials vary in their susceptibility to weathering and transport [*Menges*, 1990; *Zuchiewicz*
 125 and *McCalpin*, 2000].

126 Numerical models of extensional mountain range evolution can reproduce classic
 127 landforms such as facets, spurs, and wineglass-shaped valleys, but models differ in their
 128 representation of the governing processes. *Densmore et al.* [1998] and *Ellis et al.* [1999]
 129 introduced a model that included rock weathering, regolith creep, and bedrock lands-
 130 liding, and explored a part of the parameter space in which facet erosion occurred pri-
 131 marily by landsliding. A model developed by *Petit et al.* [2009] represented hillslope ero-
 132 sion using a diffusion formulation, with a higher transport coefficient applied to slopes
 133 steeper than 40°. In their study of facets in the Great Basin, *DePolo and Anderson* [2000]
 134 showed that the observed relationship between slip rate and facet angle was consistent
 135 with a nonlinear diffusion model. Similarly, analysis of facets along the Wasatch fault
 136 system by *Struble et al.* [in review] suggested a nonlinear relationship between erosion

rate and facet angle. The planform landscape evolution model studied by *Petit et al.* [2009] showed little correlation between facet slope and fault dip angle, whereas the geometrical analysis of *Tucker et al.* [2011] implies that fault dip should be a primary control. In summary, the community has developed several published models of extensional footwall evolution, but the implications of these models for facet evolution differ depending on the assumed process rules. To make further progress, we need models that can account for the observed diversity in facet morphology, including variations in slope angle, regolith cover, and shape, and that make field-testable predictions about the relationship between morphology, erosion rate, and slip rate.

3 Approach and Scope

We view normal-fault facets as unique natural experiments: slopes that are born as steep, seismo-tectonic fault scarps, and undergo progressive weathering and erosion as they are translated upward and away from the fault trace. We use a process-oriented cellular automaton model of facet cross-section evolution as an interpretive tool with which to address the following questions: can the model that combines rock weathering with disturbance-driven soil creep account for the observed range in facet angle, regolith cover fraction, shape, and colluvial wedge angle? If so, what are the primary controlling factors? Does the model imply a systematic relationship between facet angle and erosion rate, and if so what does that relationship look like? The answer to this last question is especially important, because it sets up a testable prediction: facet angle is easy to measure, and erosion rate can in principle be obtained either through the geometric method summarized in Figure 2 (if fault slip rate is known), or by techniques such as cosmogenic nuclide analysis.

Our focus is on the cross-sectional geometry of facets, rather than their full three-dimensional (3D) form; in other words, our interest is not in explaining why facets are often triangular (which seems to be well understood), but rather in understanding what sets their gradient, shape, and regolith cover. That said, the influence of facet length—the distance between the fault trace and the facet's upper edge at a particular cross-sectional position—is considered by comparing models with varying domain length, as described below. We do not consider controls on the height of the facet edge, as this clearly depends in part on the spacing between transverse channels, and on the topography of valley side slopes along them.

169 A cellular automaton model might seem like an odd choice for modeling the evo-
 170 lution of an idealized hillslope cross section. After all, most models of hillslope cross-sectional
 171 morphology are built on differential equations, which are sometimes viewed as “the keys
 172 to geomorphic nirvana” [Bras *et al.*, 2003]. In this case, however, it is the only model
 173 we know of that can account for both smooth, soil-mantled slopes, and steep, irreg-
 174 ular, rocky ones—and the transition between these forms [Tucker *et al.*, 2018]. More-
 175 over, the cellular framework allows a fully two-dimensional representation (as opposed
 176 to the more common profile representation, in which surface elevation is a function of
 177 one independent spatial dimension), and it provides a natural way to treat combined ver-
 178 tical and horizontal tectonic offset. Finally, the cellular approach described below (and
 179 in greater detail by Tucker *et al.* [2018]) honors the occurrence of a patchy or otherwise
 180 incomplete regolith cover, as is observed on some facet surfaces.

181 Section so-and-so does X, then Y, etc...

182 4 Cellular Hillslope Evolution Model

183 The facet profile evolution model builds on “Grain Hill” cellular automaton frame-
 184 work [Tucker *et al.*, 2018], with the addition of a 60° dipping normal fault. Advantages
 185 of the Grain Hill model include the ability to reproduce a range of hillslope forms, from
 186 soil mantled to rocky; representation of short-range and long-range (“nonlocal”) sedi-
 187 ment motion, depending on topography; direct treatment of stochastic disturbance; and
 188 ability to relate model parameters to the more commonly used transport and weather-
 189 ing rate coefficients. The model domain consists of a lattice of hexagonal cells that rep-
 190 resents a vertical cross-section through a hypothetical facet and its adjacent colluvial wedge
 191 (Figure 3). The lower left corner of the model represents a longitudinal stream that re-
 192 moves any debris delivered to it, and whose elevation is fixed to the hangingwall block,
 193 which serves as the reference frame for the model. The right side of the model represents
 194 the upper edge of the facet at that particular cross-section; increasing or decreasing the
 195 width of the domain equates to moving the cross section toward or away from the facet
 196 tip (Figure 3).

197 Each hexagonal model cell represents one of three types of material: air, rock, or
 198 regolith (Figure 4). Regolith cells may be stationary, or may be in a state of motion in
 199 one of the six lattice directions. Collectively, these materials and motion directions are

represented by assigning one of nine integer state codes to each cell in the domain. Stochastic, pairwise transitions represent the processes of rock weathering, regolith disturbance, and ensuing regolith motion [Tucker *et al.*, 2016, 2018]. For example, the rock cell in rock-air pair has a user-specified probability per unit time of transitioning to a regolith cell, representing weathering. Instead of clicking through a series of time steps of fixed duration, the model iterates over a sequence of these stochastic transitions, in which one or both cells in an adjacent pair changes state. The algorithm works by scheduling each potential transition event at a randomly generated future time, using an exponential probability distribution function of inter-event waiting times. The program then iterates in chronological order through these scheduled events. As the domain evolves, new transitions are scheduled, and some previously scheduled ones are invalidated. Tucker *et al.* [2016] provide further details on the continuous-time stochastic framework and the algorithms that implement it.

Tucker *et al.* [2018] present the rule set for the Grain Hill model. Here, we briefly summarize these rules, and describe two additions to the version they present: the implementation of periodic slip on a 60° dipping normal-fault, and the addition of a rule that represents dissolution of bedrock.

To represent normal-fault slip, a 60° -dipping fault crosses the grid lattice at a user-specified location (Figure 3, bottom). Cells in the footwall block are shifted up and to the right on a 60° angle, at a distance of $\sqrt{3}$ lattice units per time interval τ . The slip rate is therefore $V = \sqrt{3}\delta\tau$, where δ [L] is the width of a grid cell.

Production of moveable regolith from bedrock is represented by a transition from a rock-air pair to a regolith-air pair (Figure 4a,b). The rate constant w [1/T] represents the average transition frequency. Given a cell width of δ , the expected bare-bedrock weathering rate is $2\delta w$ (the factor of two reflects the fact that for a planar surface, the hex lattice geometry exposes an average of two faces per cell).

In order to explore the case of fully weathering-limited slopes, we introduce a second weathering rule to represent dissolution. When this rule is invoked, rock-air cell pairs transition to air-air pairs—representing rock dissolution—with an average rate s [1/T]. The expected bare rock dissolution rate [L/T] is therefore δs .

We assume that regolith transport can occur by two means: (1) displacement by a disturbance event and subsequent motion, or (2) spontaneous gravitational failure, when the local angle of repose is exceeded. The model's disturbance rule represents the action of processes like animal burrowing, frost heave, tree throw, and other mechanisms that tend to displace regolith outward from the surface. The disturbance transition rule applies to locations where a resting regolith cell lies adjacent to an air cell. When the transition occurs, regolith and air cell trade places, and the regolith state switches from resting to moving in the direction from which disturbance originated (Figure 4b,c). The disturbance rate parameter, d [1/T], represents the average disturbance frequency, and functionally equates to the disturbance frequency parameter N_a in the probabilistic theory of soil creep developed by *Furbish et al.* [2009]. *Tucker et al.* [2018] show that for relatively gentle slopes, the disturbance rate relates directly to the commonly used soil transport efficiency factor (“hillslope diffusivity”), D_s , according to

$$d = \frac{D_s}{60\delta^2}. \quad (2)$$

For regolith-mantled slopes steeper than about 15°, the effective transport efficiency increases progressively with slope angle, diverging at a 30° effective angle of repose [*Tucker et al.*, 2018, , their Figure 10].

Moving particles follow a set of transition rules that mimic the kinematics of inelastic grain motion in a gravitational field. Although these motion and collision rules are necessarily heuristic, they effectively capture the settling motion of disturbed particles [*Furbish et al.*, 2009]. The motion, gravitational, and inelastic collision rules are illustrated in Figure 4, and described in greater detail by *Tucker et al.* [2016] and *Tucker et al.* [2018]. One rule to note in particular: a regolith cell that lies above and adjacent to an air cell can transition to a moving state, with a high transition rate parameter. Because of the lattice geometry, this rule imposes an effective 30° angle of repose.

Sensitivity experiments indicate that the exact nature of the motion and settling rules is not especially important. What matters more is that there exists a time-scale separation between disturbance (with intervals on the order of years) and settling (time scale on the order of seconds or less). The rule set described above can capture a range of slope forms, including regolith-mantled and convex-upward forms, planar angle-of-repose, and partially mantled “rocky” slopes [*Tucker et al.*, 2018].

This generality makes the model an appropriate one for exploring bedrock fault scarps and facets, which emerge during earthquakes as steep, rock slopes, and can subsequently evolve into partially or fully regolith mantled erosional slopes. In the following section, we present model experiments that address three related questions:

1. What conditions are both necessary and sufficient to produce planar facet profiles with a thin mantle (continuous or discontinuous) of regolith?
2. Can the model account for the observed range in facet slope angle, cross-sectional shape, soil cover, and facet-to-colluvial-wedge transition?
3. What is the predicted relationship between facet gradient and erosion rate?

We explore these questions with a systematic parameter exploration, beginning with the simple case of a purely weathering-limited slope.

5 Results

5.1 Weathering Limited Case: Facet Dissolution

We start with a simple test: if a facet erodes at a steady, uniform rate, its evolution should follow the geometry illustrated in Figure 2. The profile should be linear, and the dip angle should relate to the rates of erosion and slip according to equation (1). To perform this test, we run the model with dissolution activated, and without any rock-to-regolith conversion. The expected average rate of erosion by dissolution is $E = 2\delta s$. To simplify the analysis, we define a dimensionless dissolution efficiency as

$$S' = \frac{2\delta s}{V}. \quad (3)$$

The expected facet dip angle is

$$\theta = \alpha - S', \quad (4)$$

where θ and α are both in radians. Figure 5 presents simulated profiles for facets eroded by dissolution, under different values of dimensionless weathering rate S' . The figure also compares narrow and wide facets. The simulated facets show a linear relation between angle and dissolution rate, consistent with the analytical expectation (equation 1) (Figure 6).

[ADD PREDICTED DIP ANGLES TO THE 4 DISSOLUTION PLOTS]

286 [start with section to demonstrate that tests ability of model in purely weathering-
 287 limited configuration to reproduce geometric model of Tucker 2011; add to the figure a
 288 couple of runs demonstrating change in width]

289 **IV. Results**

290 **A. Weathering-limited facets**

291 demonstrate that one recaptures Tucker et al. 2011 behavior when $d' \ll w'$: ex-
 292 periments in which the predicted angle should be 60 degrees (no weathering), 45, 30, 15.

293 **B. Influence of d' and w'**

294 3x3 (or maybe 5x5) plot in d' and w' space

295 plot of facet dip angle in d' and w' space (from talk, showing family of curves)

296 **C. (optional) what if rock or soil can dissolve, a la Italian carbonates? (dissolution
 297 rule)**

298 **D. (optional) baselevel effects - what happens when either you have a basal stream
 299 cutting down or a hangingwall valley aggrading? This would require having a modifi-
 300 cation that would add or remove rock cells along the left edge**

301 **E. what sets the effective E vs S relation? refer back to T et al., 2011, noting re-
 302 strictive assumption of slope-independent erosion rate**

303 **F. (optional) how could one mimic the effective rule in a differential equation world?
 304 Try out something like the depth-dependent Taylor model.**

305 **V. Discussion**

306 - model accounts for basic morphology and shape. necessary and sufficient condi-
 307 tions for planar facet with dip angle less than fault dip: weathering of rock plus distur-
 308 bance, and [something about limits, i.e., curvature appears when $d'/w' > ...$]

309 - facet angle close to angle of repose is an attractor state, because below that an-
 310 gle, the transport rate and length scale of produced regolith goes way down

311 - for this reason, it should be common to observe cases where the fault trace cuts
 312 across a roughly uniform slope, marking a transition from eroding rock to aggrading col-
 313 luvium

314 - cases that do NOT show this morphology are anomalies, likely reflecting strong
315 baselevel control apart from simply fault slip (aggradation or incision)

316 - facet dip angle is set by ...

317 - facet soil cover depth and spatial continuity set by ...

318 - facets are predicted to become concave-up when ...

319 - to test these ideas, we need cosmos on facet slopes!

320 VI. Conclusions

321 model accounts for facet morphology as a consequence of tectonic motion, rock weathering
322 and regolith disturbance

323 variations in facet morphology can be explained as a consequence of ...

324 erosion rate does depend on slope gradient, like thus-and-such

325 need cosmos to test these predictions

326 TENTATIVE LIST OF FIGURES:

327 - pix of facets

328 o bar graph of regolith thickness and percent cover on a bunch of facets

329 - model illustration combining list of states with hexagons, with schematic example
330 transitions from Grain Hill

331 - T et al 2011 schematic

332 = figure showing model diss-lim runs at varying S', compared with analytical

333 - model vs analytical diss-lim

334 - 4x4 of sim profiles in d' vs w' space

335 - plot of gradient in d' and w' space

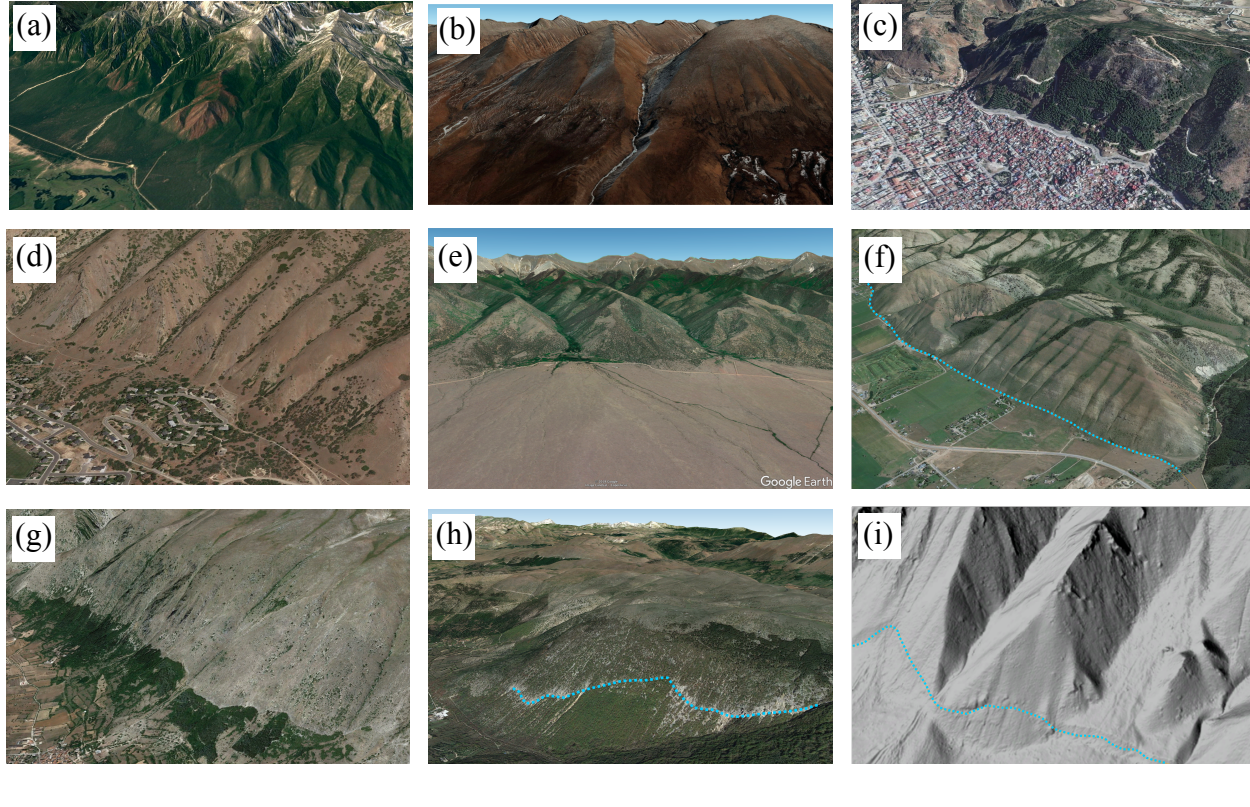
336 - same for reg cover proportion

337 (o illustration with baselevel lowering)

338 - illustration with baselevel rise

339 o illustration with time-varying w and/or d

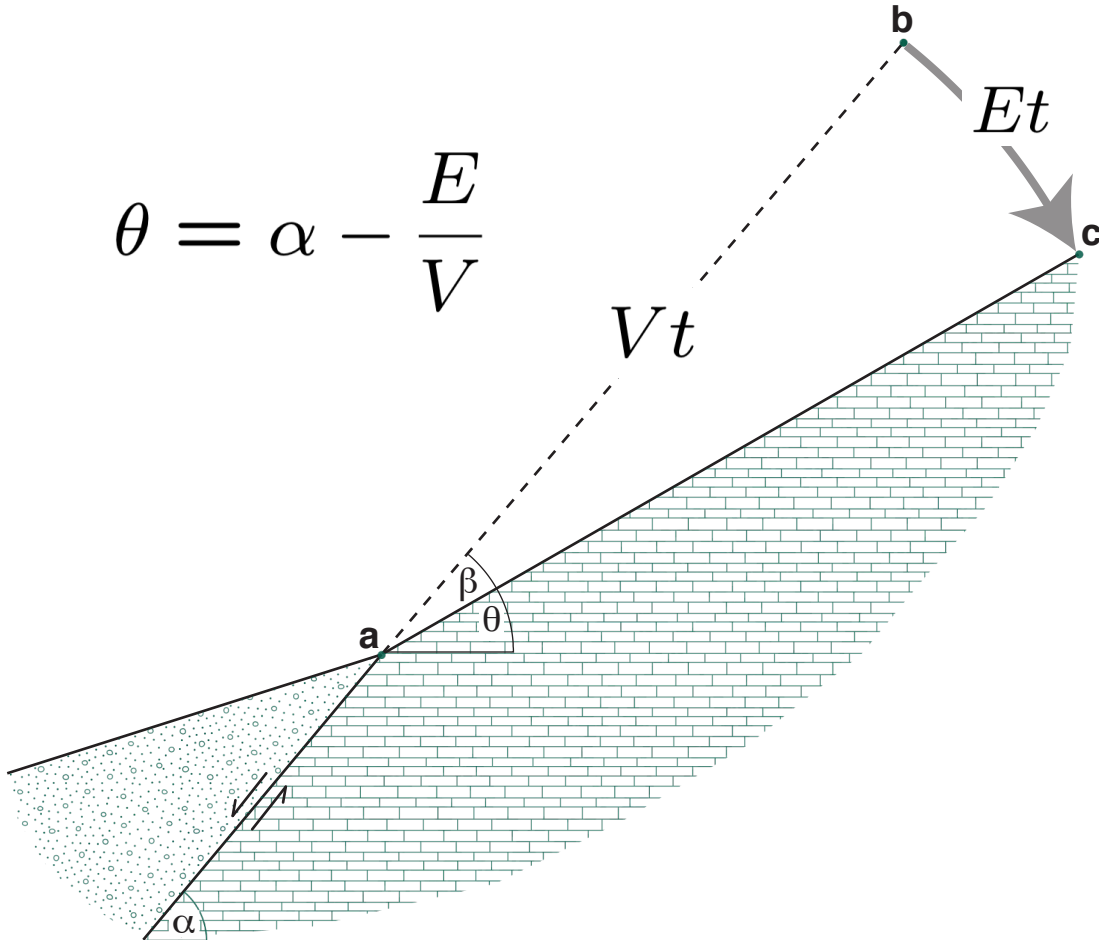
$$\alpha - \theta = E/V \quad (5)$$



340 **Figure 1.** Examples of normal-fault facets. (a) mountain front in Lake Baikal Rift Zone,
 341 Russia. (b) Kung Co half graben, Tibet. (c) Hatay Graben, Antakya, Turkey [Boulton and Whit-
 342 taker, 2009]. (d) Wasatch fault system, Provo section, near Springville, Utah, USA. (e) west
 343 side of Sangre de Cristo range, San Luis Valley, Colorado, USA. (f) Star Valley fault, Wyoming,
 344 USA. Note fault trace (light blue dotted line) at base of range front. (g) Magnola fault, central
 345 Apennines, Italy. Vegetation break marks approximate location of fault trace. (h) Portion of the
 346 Fucino fault near Gioi di Marsi, Italy. Fault trace shown in light blue dotted line. (i) Wasatch
 347 fault system, Nephi section, Utah, USA. Fault trace shown in light blue dotted line.

381 Acknowledgments

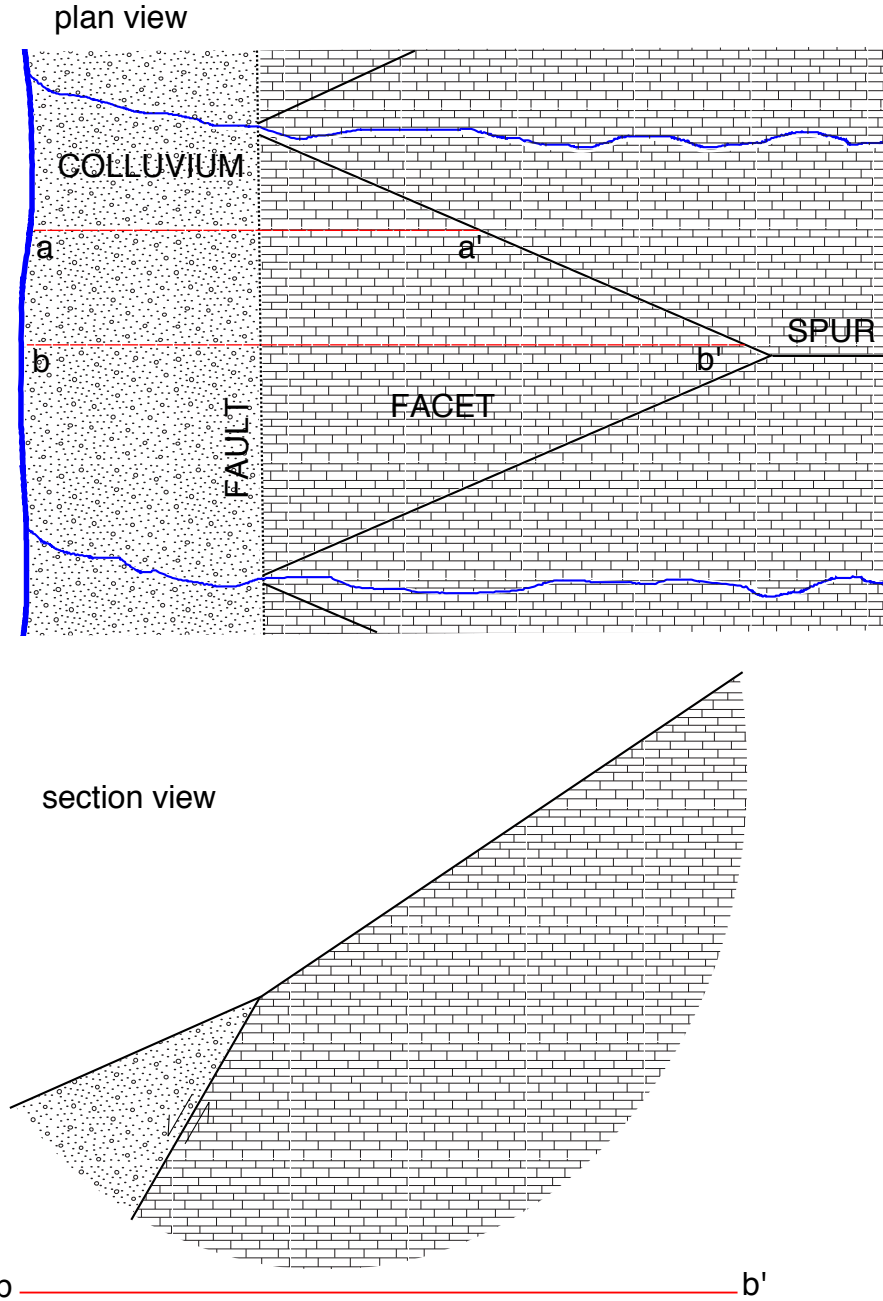
382 NSF normal faults, landlab, csdms, ...



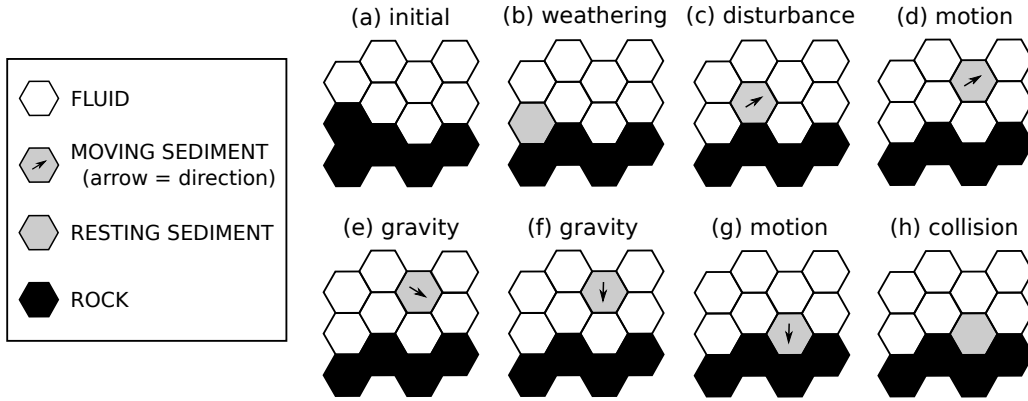
348 **Figure 2.** Conceptual illustration showing how fault slip rate, V , fault dip angle, α , and facet
 349 erosion rate, E , combine to set the dip angle of a facet profile. (Modified from Tucker *et al.*
 350 [2011].)

383 References

- 384 Anderson, T. C. (1977), Compound faceted spurs and recurrent movement in the
 385 Wasatch Fault zone, north central Utah, Ph.D. thesis, Brigham Young University.
 386 Blackwelder, E. (1928), The recognition of fault scarps, *The Journal of Geology*,
 387 36(4), 289–311.
 388 Boulton, S., and A. Whittaker (2009), Quantifying the slip rates, spatial distribution
 389 and evolution of active normal faults from geomorphic analysis: Field examples
 390 from an oblique-extensional graben, southern Turkey, *Geomorphology*, 104(3-4),
 391 299–316.

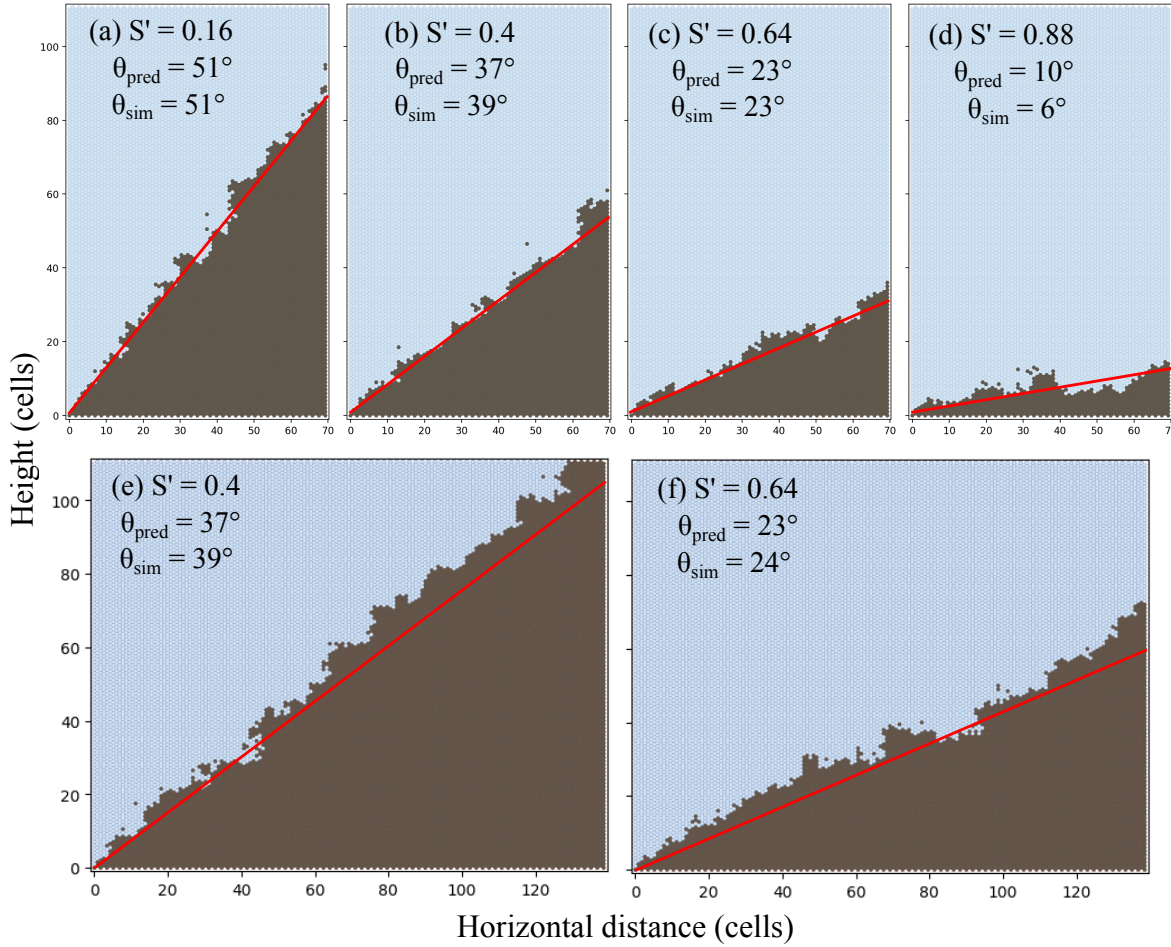


351 **Figure 3.** Schematic illustration of model domain, which represents vertical cross-section
 352 through an idealized facet and its adjacent colluvial wedge (a–a'). Right side of domain repre-
 353 senters the upper edge of facet, and left side represents a longitudinal stream in the hangingwall
 354 that removes any debris delivered to it. Changing the position of the cross section (for example,
 355 from a–a' to b–b'), and therefore its length, is accomplished by changing the width of the model
 356 domain.



357 **Figure 4.** Illustration of cell states and pairwise transitions in the Grain Facet model. Each
 358 cell assigned an integer from 0 to 8 that represents its state (0 is fluid, states 1–6 represent the
 359 six directions of motion, state 7 is resting sediment, and state 8 is rock). (Figure modified from
 360 *Tucker et al. [2018]*).

- 392 Bras, R., G. Tucker, and V. Teles (2003), Six myths about mathematical model-
 393 ing in geomorphology, in *Prediction in Geomorphology*, edited by P. Wilcock and
 394 R. Iverson, pp. 63–79, American Geophysical Union.
- 395 Bubeck, A., M. Wilkinson, G. P. Roberts, P. Cowie, K. McCaffrey, R. Phillips, and
 396 P. Sammonds (2015), The tectonic geomorphology of bedrock scarps on active
 397 normal faults in the Italian Apennines mapped using combined ground penetrating
 398 radar and terrestrial laser scanning, *Geomorphology*, 237, 38–51.
- 399 Davis, W. M. (1903), The mountain ranges of the great basin, *Harvard University*
 400 *Museum of Comparative Zoology Bulletin*, 40(3), 129–177.
- 401 Davis, W. M. (1909), *Geographical Essays*, Ginn.
- 402 Densmore, A. L., M. A. Ellis, and R. S. Anderson (1998), Landsliding and the evo-
 403 lution of normal-fault-bounded mountains, *Journal of Geophysical Research*, 103,
 404 15,203–15,219.
- 405 DePolo, C., and J. Anderson (2000), Estimating the slip rates of normal faults in the
 406 great basin, USA, *Basin Research*, 12(3–4), 227–240.
- 407 Ellis, M., A. Densmore, and R. Anderson (1999), Development of mountainous to-
 408 pography in the Basin Ranges, USA, *Basin Research*, 11(1), 21–42.
- 409 Fuller, R. E. (1931), The geomorphology and volcanic sequence of Steens Mountain
 410 in southeastern Oregon, *University of Washington Publications in Geology*, 3(1).



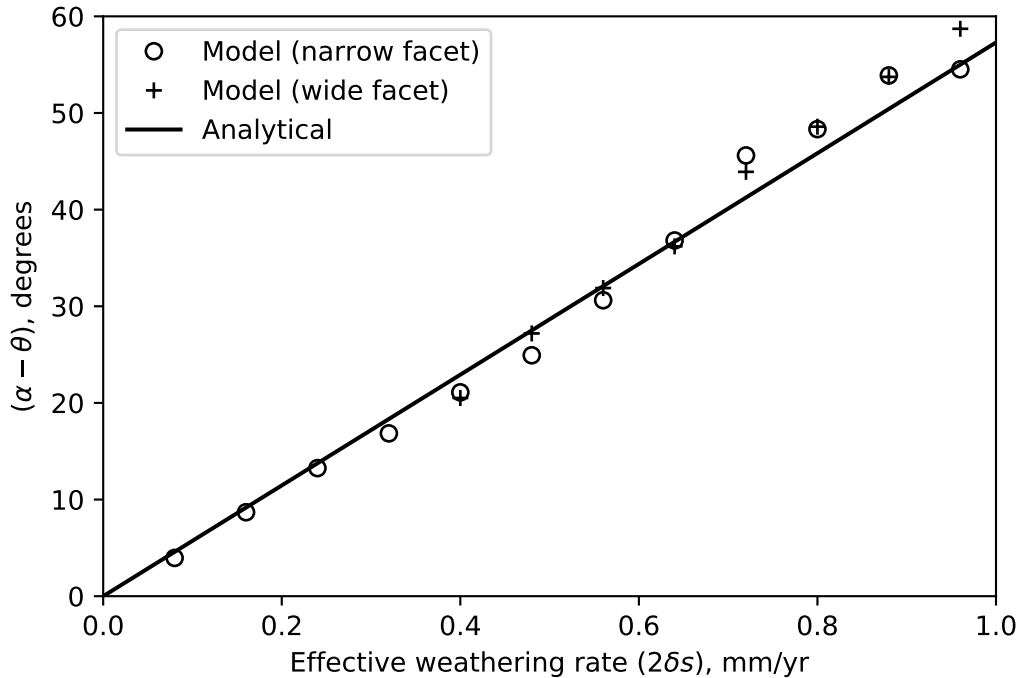
361 **Figure 5.** Simulated facet cross-sectional profiles formed under a combination of fault slip
 362 and dissolution. Dark gray indicates rock, and light blue is air. Labels show the dimensionless
 363 effective dissolution efficiency, S' (equation 3), and the predicted and simulated average facet
 364 slope angle, θ . Line shows facet profile predicted by equation (4).

411 Furbish, D., P. Haff, W. Dietrich, and A. Heimsath (2009), Statistical description of

412 slope-dependent soil transport and the diffusion-like coefficient, *J. Geophys. Res.*,
 413 114, F00A05.

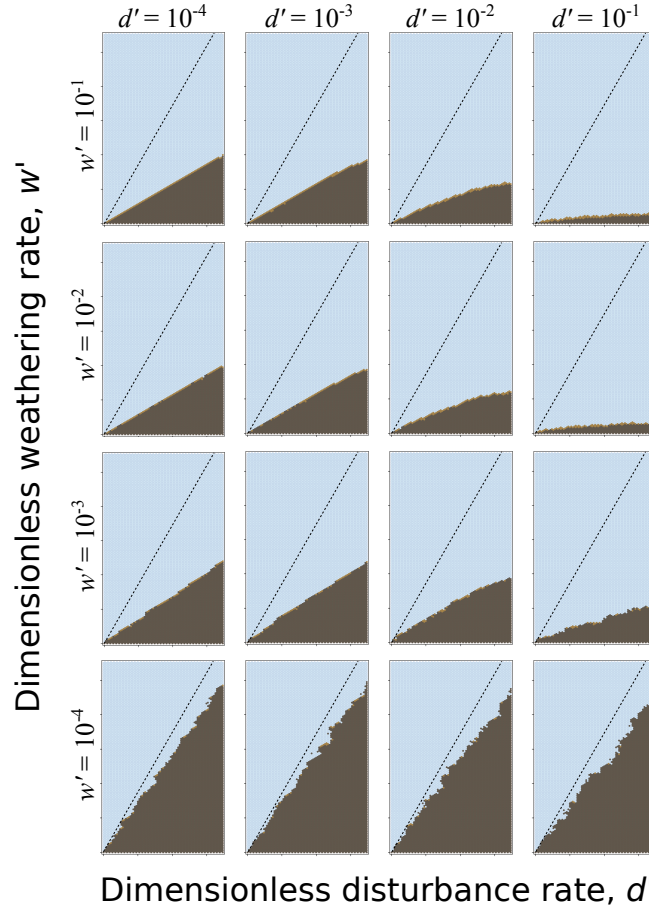
414 Gilbert, G. (1928), *Studies of basin-range structure*, U. S. Geological Survey Profes-
 415 sional Paper, vol. 153, United States Government Printing Office.

416 Gilluly, J. (1928), Basin range faulting along the Oquirrh Range, Utah, *Bulletin of*
 417 *the Geological Society of America*, 39(4), 1103–1130.



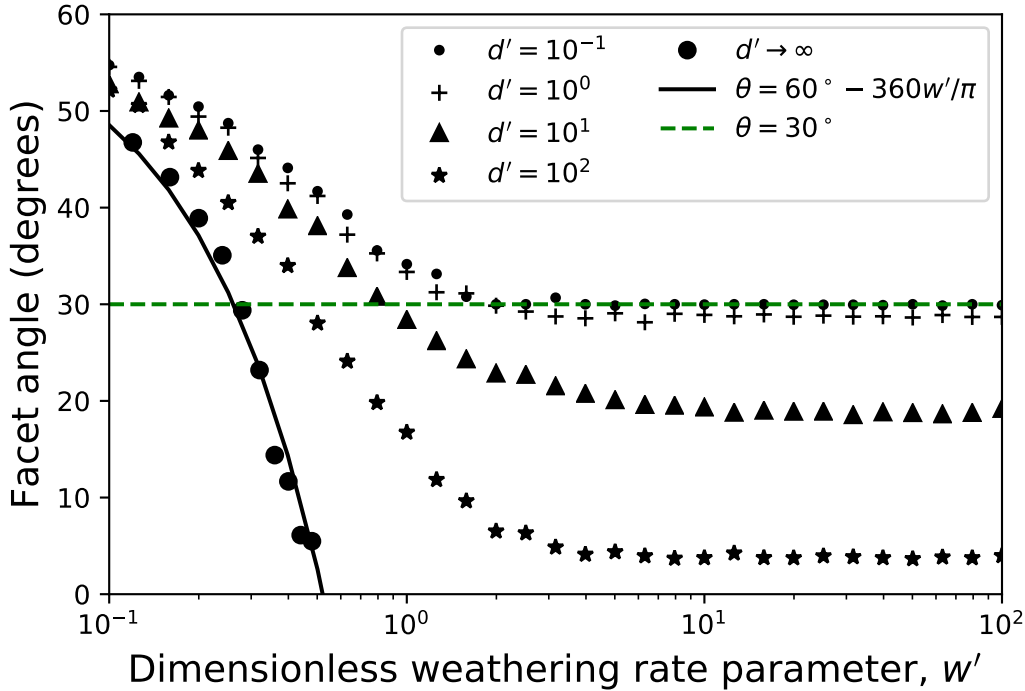
365 **Figure 6.** Difference in angle between fault plane (α) and facet (θ), as a function of the
 366 nominal dissolution rate $2\delta s$, from runs with fault slip and dissolution (only). Open circles and
 367 plusses show individual model runs with a narrow and wide horizontal domain, respectively (see
 368 Figure 5). Line shows the prediction of equation 5.

- 418 Hamblin, W. (1976), Patterns of displacement along the wasatch fault, *Geology*,
 419 4(10), 619.
- 420 Menges, C. (1990), Soils and geomorphic evolution of bedrock facets on a tectoni-
 421 cally active mountain front, western Sangre de Cristo Mountains, New Mexico,
 422 *Geomorphology*, 3(3-4), 301–332.
- 423 Pack, F. J. (1926), New discoveries relating to the Wasatch fault, *American Journal*
 424 *of Science*, 11(65), 399–410.
- 425 Petit, C., Y. Gunnell, N. Gongga-Saholiariliva, B. Meyer, and J. Seguinot (2009),
 426 Faceted spurs at normal fault scarps: Insights from numerical modeling, *Journal*
 427 *of Geophysical Research—Solid Earth*, 114, doi:10.1029/2008JB005955.
- 428 Schneider, H. (1925), A discussion of certain geologic features of the Wasatch Moun-
 429 tains, *The Journal of Geology*, 33(1), 28–48.



369 **Figure 7.** Examples of simulated facet profiles at varying values of d' and w' . Dotted line
 370 shows projected fault plane.

- 430 Strak, V., S. Dominguez, C. Petit, B. Meyer, and N. Loget (2011), Interaction be-
 431 tween normal fault slip and erosion on relief evolution: Insights from experimental
 432 modelling, *Tectonophysics*, 513(1-4), 1–19.
 433 Struble, W. T., S. W. McCoy, D. E. J. Hobley, G. E. Tucker, and L. C. Gregory (in
 434 review), Mountain-Front Facet Gradient Encodes Long-Term Slip Rate Along the
 435 Wasatch Normal Fault, USA, *TBD*.
 436 Tucker, G., S. McCoy, A. Whittaker, G. Roberts, S. Lancaster, and R. Phillips
 437 (2011), Geomorphic significance of postglacial bedrock scarps on normal-fault
 438 footwalls, *Journal of Geophysical Research*, 116(F1), F01,022.
 439 Tucker, G. E., D. E. Hobley, E. Hutton, N. M. Gasparini, E. Istanbulluoglu, J. M.
 440 Adams, and S. S. Nudurupati (2016), Celllab-cts 2015: continuous-time stochas-
 441 tic cellular automaton modeling using landlab, *Geoscientific Model Development*,



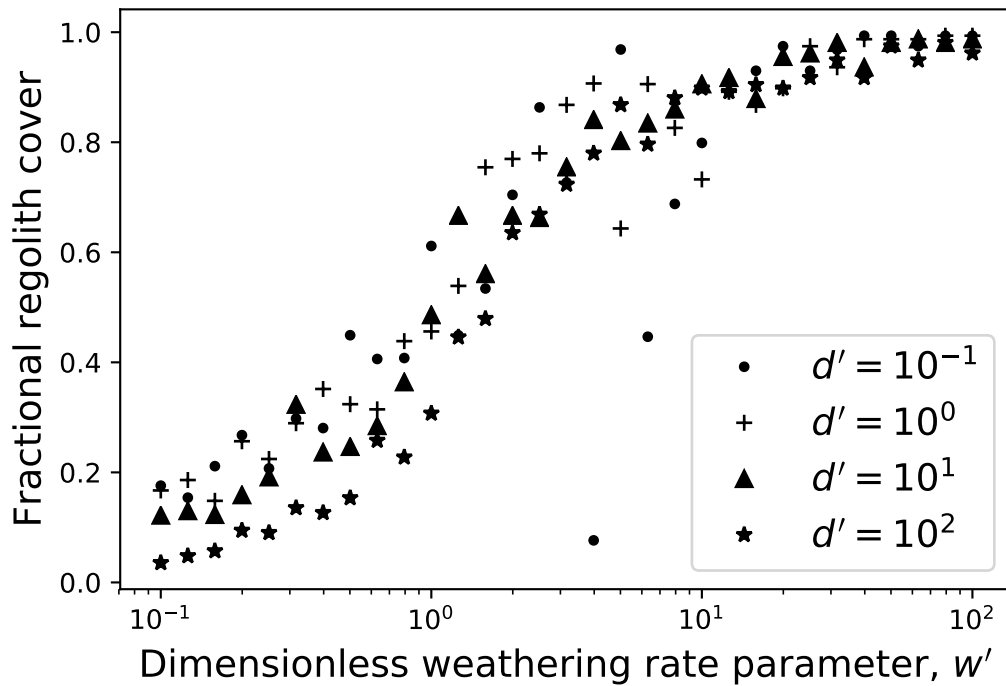
371 **Figure 8.** Modeled equilibrium facet angle as a function of weathering and disturbance rate
 372 parameters. Solid line shows the analytical solution for the case in which no regolith is produced
 373 (all rock dissolves), which corresponds to an effectively infinite disturbance rate. Dashed line
 374 shows the model's 30° effective angle of repose.

442 9(2), 823–839.

443 Tucker, G. E., S. W. McCoy, and D. E. Hobley (2018), A lattice grain model of
 444 hillslope evolution, *Earth Surface Dynamics*, 6(3), 563–582.

445 Wallace, R. (1978), Geometry and rates of change of fault-generated range fronts,
 446 north-central Nevada, *Journal of Research of the U.S. Geological Survey*, 6(5),
 447 637–650.

448 Wilkinson, M., G. P. Roberts, K. McCaffrey, P. A. Cowie, J. P. F. Walker, I. Pa-
 449 panikolaou, R. J. Phillips, A. M. Michetti, E. Vittori, L. Gregory, et al. (2015),
 450 Slip distributions on active normal faults measured from LiDAR and field map-
 451 ping of geomorphic offsets: an example from L'Aquila, Italy, and implications for
 452 modelling seismic moment release, *Geomorphology*, 237, 130–141.



375 **Figure 9.** Modeled regolith cover proportion for steady facets, as a function of weathering and
 376 disturbance rate parameters. Scatter around the sigmoidal curve reflects stochastic variability.

453 Zuchiewicz, W. A., and J. P. McCalpin (2000), Geometry of faceted spurs on an
 454 active normal fault: case study of the central wasatch fault, utah, usa, in *Annales*
 455 *Societatis Geologorum Poloniae*, vol. 70, pp. 231–249.

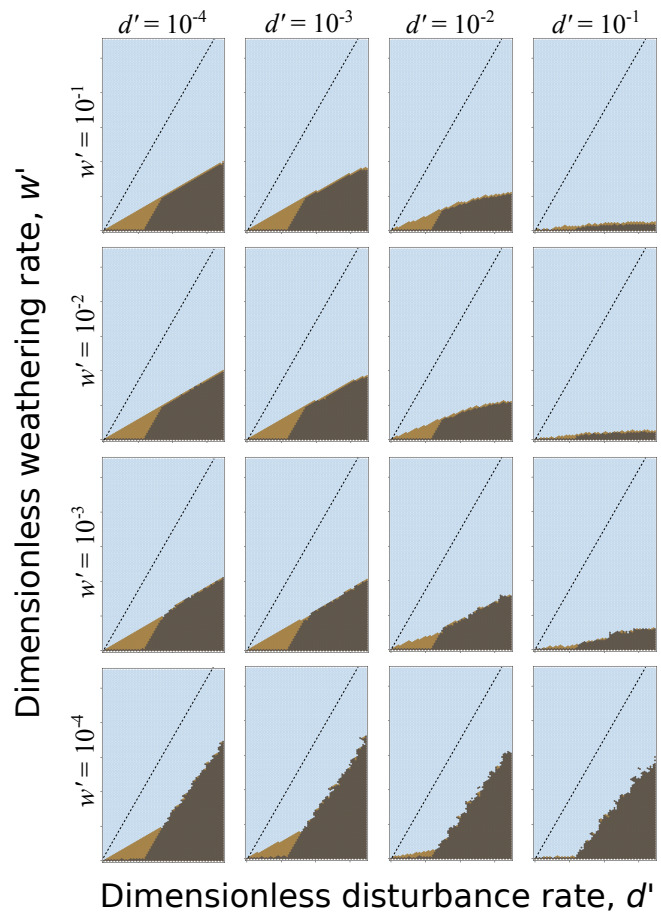
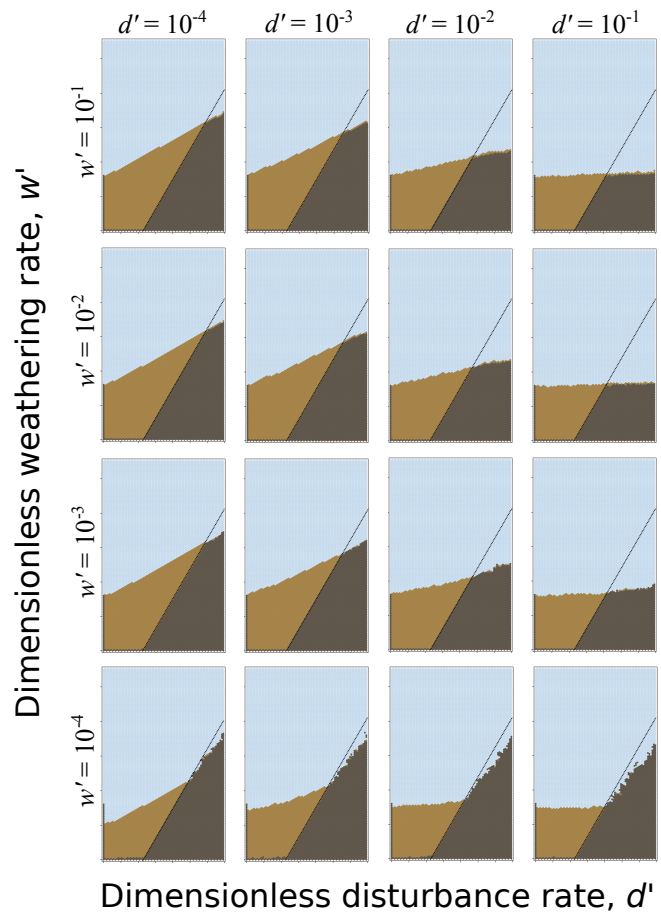


Figure 10. Simulated facet profiles showing the development of a colluvial wedge on the hangingwall.
377
378



379 **Figure 11.** Simulated facet profiles with a rising baselevel along the left model boundary,
 380 representing an aggrading hangingwall basin.